Journal of Wind Engineering & Industrial Aerodynamics 232 (2023) 105246

Contents lists available at ScienceDirect

Journal of Wind Engineering & Industrial Aerodynamics

journal homepage: www.elsevier.com/locate/jweia

Comparison and uncertainty quantification of roof pressure measurements using the NIST and TPU aerodynamic databases

Erick Shelley [a], Erin Hubbard [b], Wei Zhang [a,*]

[a] *Mechanical Engineering Department, Cleveland State University, 1960 East 24th Street, Cleveland, OH 44115, United States of America*
[b] *HX5 Sierra, LLC, 21000 Brookpark Rd, Cleveland, OH 44135, United States of America*

ARTICLE INFO

Keywords:
Boundary-layer (BL) wind tunnel
Data inconsistency
Monte Carlo simulation
Roof pressure coefficient
Uncertainty quantification

ABSTRACT

The pressure coefficient of a low-rise building in the ASCE wind load design provision is usually obtained from boundary-layer wind-tunnel tests. Although these tests tend to be standardized, inconsistent results from different facilities have been acknowledged as a long-standing issue. This work compares roof pressure for a low-rise building model archived in the National Institute of Standards and Technology (NIST) aerodynamic database and the Tokyo Polytechnic University database, followed by quantifying the measurement and data reduction uncertainties of the NIST datasets. The Monte Carlo simulation propagates four elemental uncertainties to the mean $\overline{C_p}$, standard deviation C_p' and peak pressure coefficient $C_{p,peak}$. Results indicate that pronounced differences in the roof pressure from two datasets are attributed to different inflow characteristics (including the Jensen number variation) and the inherent measurement uncertainties. High measurement uncertainties of $\overline{C_p}$ and $C_{p,peak}$ are strongly correlated with vortical flow structures, either separated flow or conical vortices at the roof corner and windward edges. Two dominant measurement uncertainty sources are distinguished: the dynamic pressure ratio uncertainty and the surface pressure tap uncertainty. Alternative flow and pressure measurement techniques are noted to potentially reduce the two dominant uncertainty sources. This work is intended to clarify measurement uncertainty sources of obtaining pressure coefficients in wind-tunnel model tests and shed lights on why large differences exist from different tests.

1. Introduction

Boundary-layer (BL) wind-tunnel tests of wind loading on building models have served as the primary means to determine the minimal design wind loads by the American Society of Civil Engineers (ASCE) provisions. Wind-tunnel tests create a controlled, simulated boundary-layer flow condition and scaled building models are used to reproduce the wind structure interaction that is of interest. For wind load tests, the essential measurement quantities include local surface pressure and/or overall forces and moments, as well as the inflow properties (wind speed profiles, turbulence intensities and power spectrum) that a model is subjected to. Wind loads for building design (including the main structure and building components) in the ASCE wind codes are specified as,

$$F_a = q \cdot Cp \cdot C_e \cdot C_g \cdot A, \tag{1}$$

where F_a is the wind load, q is the dynamic wind pressure, C_e and C_g are the terrain exposure and wind gust factors, A is the nominal tributary area, and Cp is the pressure (or load) coefficient. This seemingly simple equation links the local wind climate, the wind loads, and the structure's dynamic response to the wind — "Alan G. Davenport Wind Loading Chain" (Kareem and Tamura, 2013). Pressure coefficient C_p for a typical building type is usually measured by boundary-layer (BL) wind-tunnel tests. BL wind-tunnel model tests have advanced the wind loading design in the past few decades (Holmes, 1988; Surry, 1991; Letchford, 2001; Cermak, 2003; Tieleman, 2003; Cochran, 2006; Endo et al., 2006; Fernández-Cabán and Masters, 2018) and will continue doing so in the foreseeable future. However, it is well known that pressure coefficients on scaled building models often show pronounced discrepancies from different wind-tunnel tests. As reported by Fritz et al. (2008), the variability of wind effects indicated in peak negative pressure coefficient ranges from 10% to 30% for wind directions of 0° and 90° based on tests at six renowned wind tunnel laboratories. Indeed, such tests are guided by standards (Cermak et al., 1999; Simiu et al., 2009), and significant efforts are put in model preparation, experimental setup, equipment/instrumentation calibration, and data reduction methodology. There is a need for a detailed analysis of what caused the large variability and uncertainties that could improve estimation of wind load factors.

---

* Corresponding author.
E-mail addresses: e.shelley@vikes.csuohio.edu (E. Shelley), erin.p.hubbard@nasa.gov (E. Hubbard), w.zhang13@csuohio.edu (W. Zhang).

https://doi.org/10.1016/j.jweia.2022.105246
Received 17 March 2022; Received in revised form 31 October 2022; Accepted 16 November 2022

Uncertainties in the wind-tunnel measurements of pressure coefficients C_p are primarily in three aspects: (1) how well the simulated wind represents full-scale atmospheric boundary-layer winds; (2) to what extent the dynamic similarity is achieved (in particular, the Reynolds number range); and (3) measurement and data reduction uncertainties (Simiu and Yeo, 2019). The first two aspects are extensively discussed in the literature, such as Tieleman (2003), Cochran (2006) among others. For example, a recent work by Nandi et al. (2022) quantified the effect of uncertainty of roughness length (z_o) of upstream terrain on the estimation of structural response to wind. It was found that neglecting this uncertainty can underestimate the building response by as much as 45%. However, the measurement and data reduction uncertainties in the wind-tunnel measurements of pressure coefficients C_p have not been well understood. To address this outstanding issue and improve understanding of what caused the significant variabilities of the pressure coefficients C_p, measurement and data reduction uncertainties must be carefully examined and quantified.

Uncertainty quantifies a probabilistic interval within which a "true value" is likely to fall from the reported result (Coleman and Steele, 2018). Error sources in wind-tunnel tests can be classified into two categories: systematic or bias sources and random sources. Systematic errors create an offset from the actual value to the "nominal" value, while random errors cause a random variation typically following a Gaussian distribution about the nominal value. Distinguishing between uncertainty sources as random and systematic can be useful for researchers to determine if the resulting uncertainties will affect their results. For example, a researcher comparing the experimental results with CFD models cares about both systematic and random uncertainties, while a researcher looking for small changes in results due to model modification requires low random uncertainty but may not concern a systematic offset in their data. Random uncertainties could be evaluated and minimized by repeating the same test a sufficient number of times. Systematic errors can be compensated once correctly identified, but often it is difficult to completely separate random and systematic errors. Systematic uncertainty sources are sometimes overlooked and hard to quantify; they do not cause variation in repeatedly collected data but rather introduce biasing effects for which they are defined.

"The uncertainty is as important a part of the result as the estimate itself. … An estimate without a standard error is practically meaningless" (Jefferys 1967 in Higdon et al. 2006). Even when sources of uncertainty are acknowledged, experimentalists and researchers often publish test results without uncertainty explicitly. When reporting pressure statistics from BL wind-tunnel tests, a detailed uncertainty quantification (UQ) is often missing (Ho et al., 2005). This hinders a fair comparison among similar tests in different experimental facilities and understanding of the driving uncertainty sources introduced at different stages of wind-tunnel tests. Without uncertainty as part of the results, meaningful comparisons cannot be made between two tests, or between computational model and a test for validation purposes. Additionally, when uncertainty sources and their impacts on a result are less understood, strategies to effectively improve tests and increase the fidelity of the results remain elusive. One must also note that, owing to the complexity of data acquisition/reduction, it is often necessary to estimate uncertainties not only on the basis of measurements and statistics, but also by making somehow subjective assessments, inferences from past practices, and simplified reliability methods (Simiu and Yeo, 2019).

Despite the rapid growth of computing performance, it may take decades until the complexity of wind and structure interaction can be faithfully simulated in all details. It can be expected that full-scale experiments and wind tunnel tests of wind effects on buildings remain essential tools for better understanding flow physics, and for validation of prediction results and for assisting numerical modeling development (Scharnowski and Kähler, 2020). Since BL wind-tunnel test cases and results are increasingly used to validate computational fluid dynamics (CFD) simulation in wind engineering research, it is highly desirable to provide uncertainty quantification of the wind-tunnel test data and results. Recent results in quantifying uncertainties in CFD simulations suggest wind pressure loads on buildings can be strongly influenced by uncertainty in the inflow boundary conditions and the turbulence model. UQ presents more meaningful information to designers and engineers than the outcome of a single deterministic CFD simulation (Lamberti and Gorlé, 2018).

There are several aerodynamic databases in public domain, including the The NIST/University of Western Ontario (UWO) aerodynamics database, referred to as the UWO database, the Tokyo Polytechnic University (TPU) aerodynamic database and the NSF-sponsored DesignSafe-CI Data Depot. The UWO database archives time series of pressure coefficients at large numbers of ports on the external surface of a variety of low-rise building models (NIST, 2017). Until recently it was the largest existing aerodynamic database for low-rise building wind loading. The basic building configuration has a rectangular plane shape. Thirty-seven building models with distinct dimensions and five roof slopes and eave heights are tested. A series of publications documented the comprehensive wind-tunnel study of pressure distribution on variations of building model scale, wind directions, leakage condition, and terrain type (Ho et al., 2005; St. Pierre et al., 2005; Oh et al., 2007). The NIST aerodynamic database has been used for assessing the wind load provisions for low-rise buildings. For example, Kopp and Morrison (2018) examined component and cladding wind load provisions for low-sloped roofs on low-rise buildings using measured pressure data from the UWO database. The TPU aerodynamic database is part of the Wind Effects on Buildings and Urban Environment, the 21st Century Center of Excellence Program, 2003–2007 (Tamura, 2012). Gierson et al. (2015) utilized the TPU wind tunnel data to evaluate the ASCE 7-10 wind velocity pressure coefficients on the components and cladding of low-rise buildings. Hagos et al. (2014) examined aerodynamic pressures and forces based on the UWO and TPU data for low-rise buildings to assess the extent to which the respective aerodynamic pressure measurements are comparable. They compared three cases of gable-roof low-rise buildings (of two roof slopes and two width/depth ratios) and concluded reasonable equivalent results from these cases for practical engineering purposes. The present work is built upon (Hagos et al., 2014) to not only compare selected cases from UWO and TPU databases, but account for measurement uncertainties of the pressure coefficients obtained in the UWO datasets.

This work will look into the differences in the measured pressure coefficient statistics using data archived in the NIST and TPU aerodynamic databases. The objective of this research is two-fold: (1) To compare the mean, standard deviation of and the peak pressure coefficient of selected comparable cases in the UWO and the TPU databases; and (2) determine the measurement uncertainty and identify the primary uncertainty contributors to pressure statistics, which allows for thinking of alternative measurement techniques to potentially reduce the measurement uncertainty in similar wind-tunnel tests.

2. Case selection and analysis methodology

2.1. Low-rise building model, inflow conditions and terrain exposure

An isolated low-rise building of a nearly-flat roof (1:100 scaled, 1:12 roof pitch, no leakage model) is selected as the target building model. While ABL flows over two exposures – open and suburban terrains – are simulated in the UWO datasets, only suburban terrain is simulated in the TPU wind-tunnel tests. Therefore, test cases for suburban terrain with a roughness length of $z_o = 0.3$ m is selected from the UWO database. For a fair comparison, building geometric similarities were also considered in terms of building depth D, breadth B and eave height H (Table 1).

Table 1
Dimensions and geometric ratios of the low-rise building model of the UWO and TPU wind-tunnel tests (Ho et al., 2003; Tamura, 2012).

Database case #	Model scale	Roof slope (°)	Breadth B (m)	Depth D D (m)	Eave height H (m)	Ratio B/H	Ratio D/H	Ratio D/B
UWO (ox2)	1:100	4.76	0.49	0.76	0.12	4:1	6.25:1	3.12:2
TPU	1:100	4.8	0.16	0.24	0.04	4:1	6:1	3:2

The inflow of the simulated surface layer is characterized in terms of mean wind profiles, streamwise turbulence intensity profiles, and scaling parameters. The empirical power-law mean wind profile is commonly used in wind engineering as follows:

$$\frac{U(z)}{U(z_r)} = \left(\frac{z}{z_r}\right)^{\alpha} \tag{2}$$

where z_r is the reference height, $U(z_r)$ is the mean wind speed at the reference height, and α is the power-law exponent or the wind shear exponent. Vertical profiles of the streamwise turbulence intensity are obtained as the primary turbulence quantity. While UWO incoming wind is measured using hot-wire anemometers (HWA) which allow for turbulence scales of three dimensions as examined in Ho et al. (2005), such information is not available for the TPU wind-tunnel tests. Therefore turbulent length scales are not included in the comparison.

The flow development and pressure distribution over a roof is strongly affected by wind direction. The UWO dataset (Data Set ID ox2 (NIST, 2017)) covers 5° to 90° and 270° to 360° with a 5° interval, in total 37 wind directions. The TPU case covers 0° to 90° with an interval of 15°. We will focus on the normal wind direction of 270° (90° equivalent) to the longer side of the building and an oblique wind direction of 315° (45° equivalent). When comparing the UWO and TPU datasets, the coordinate systems of the pressure tap locations of the models are inconsistent, as seen in Fig. 1. For the convenience of comparison, a coordinate system is defined to place the origin (0,0) at the top left corner of the roof schematics and align with that of the UWO case (Fig. 1).

2.2. Data processing of time series of surface pressure

The pressure coefficient C_p datasets recorded by UWO can be accessed at the NIST Aerodynamic Database (NIST, 2017). The NIST database provides time series of pressure coefficients at the reference height $C_{p,ref}$, and at 1000 times the magnitude of the actual values. The reference height is located approximately at the halfway height of the wind tunnel, where the incoming wind velocity is uniform with low turbulence levels outside of the simulated surface layer. Data processing is required to convert $C_{p,ref}$ referenced to the upper-level dynamic pressure q_{ref} in the wind tunnel to C_p referenced to the eave height dynamic pressure q_H conventionally. This is done by the following:

$$C_p = C_{p,ref} \times \frac{q_{ref}}{q_H} = C_{p,ref} \times \left(\frac{V_{ref}}{V_H}\right)^2, \tag{3}$$

$$\frac{V_{ref}}{V_H} = \frac{V_{ref}}{V_{int}} \times \frac{V_{int}}{V_H}, \tag{4}$$

where q_{ref}/q_H is the dynamic pressure ratio of the reference height with respect to the eave height. The velocity ratio V_{ref}/V_H is not measured directly in the UWO datasets, instead obtained via an intermediate-level velocity V_{int}. The velocity measurements by pitot tubes in building model tests were conducted at the intermediate height of 0.488 m and the roof height. The intermediate level measurements are taken upstream of the turntable at the centerline and 1/4 point of the wind tunnel width, and the eave height measurements are located off the turntable to avoid model-induced disturbances. The intermediate height measurements are intended to give a reference related to upper-level wind speed measurements and serve as an overall monitor of the simulation (Ho et al., 2005).

TPU's aerodynamic database contains multiple sub-databases ranging from low-rise buildings (with and without eave) to high-rise buildings (TPU, 2012). For the selected cases of a low-rise building model, surface pressure taps were evenly distributed over the surfaces with a spacing of 20 mm. The TPU database provides the processed C_p statistics data, which are treated with a 3-point moving average (Tamura, 2012). The TPU data has a time scale 3/100 (with 3-point moving average already applied to the time series), and the UWO data has a time scale of about 6/100. At the lab scale, the UWO had sampling period of 100 s while TPU had a sampling period of 18 s with each case being sampled at 500 Hz. To be consistent, the UWO time series of pressure data are also treated with a 6-point moving average to calculate the duration of 0.2 s for the full scale so that a fair comparison between these two cases is achieved.

Mean pressure coefficient $\overline{C_p}$ and the standard deviation $C_p{}'$ are calculated using the corresponding time series of surface pressure data as follows:

$$\overline{C_p} = \frac{1}{N}\sum_{i=1}^{N} C_{p_i} \tag{5}$$

$$C_p{}' = \sqrt{\frac{1}{N-1}\sum_{i=1}^{N}(C_{p_i} - \overline{C_p})^2} \tag{6}$$

Since the pressure fluctuations are only explicitly captured for the duration of the sampling period of the wind-tunnel tests, the expected peak pressures for full-scale need to be found by considering the statistical distribution of peak pressures. Gavanski et al. (2016) studied how data duration and sampling frequency impact on the peak pressure estimation. The method adopted herein utilizes a procedure to estimate expected peak values for database-assisted design (Sadek and Simiu, 2002). Through statistical testing, this procedure determines and uses the Extreme Value Type I (Gumbel) distribution to best estimate the peak distribution, with gamma and normal distributions to estimate the longer and shorter tails of this non-Gaussian distribution. A primary and two supplemental MATLAB functions were developed by Joseph A. Main using this procedure and was used to calculate the expected peak $C_{p,peak}$ in this study.

2.3. Uncertainty quantification (UQ) procedure

The uncertainty analysis begins by determining elemental uncertainty estimates of the instrumentation used for measurements of each quantity, then determines the random and systematic uncertainties associated with particular measurements and the flow facility. As calibrations, assumptions and data reduction are made, associated uncertainties are also included in the chain, and all uncertainties are propagated to obtain the overall uncertainty of the value of interest (Stephens et al., 2016). To model how the elemental uncertainties propagate to the uncertainty of the value of interest, the Taylor series method is traditionally used, which becomes less effective when dealing with non-linear equations and dynamic systems. On the contrary, the Monte Carlo Method (MCM) of uncertainty propagation standardized in the ISO Guide's supplement (BIPM et al., 2008), is a probabilistic approach to UQ — random draws are made from assumed error distributions for all identified uncertainty sources, errors are added to appropriate seed data values to simulate measured data, and then perturbed data are reduced to results of interest (Coleman and Steele, 2018). Random numbers based on the statistical distribution of each uncertainty source are generated for the time series data. The errors are then propagated and reduced to the C_p statistics (Stephens et al., 2016). The standard deviations of these parameters of interest are calculated, representing the standard uncertainty obtained

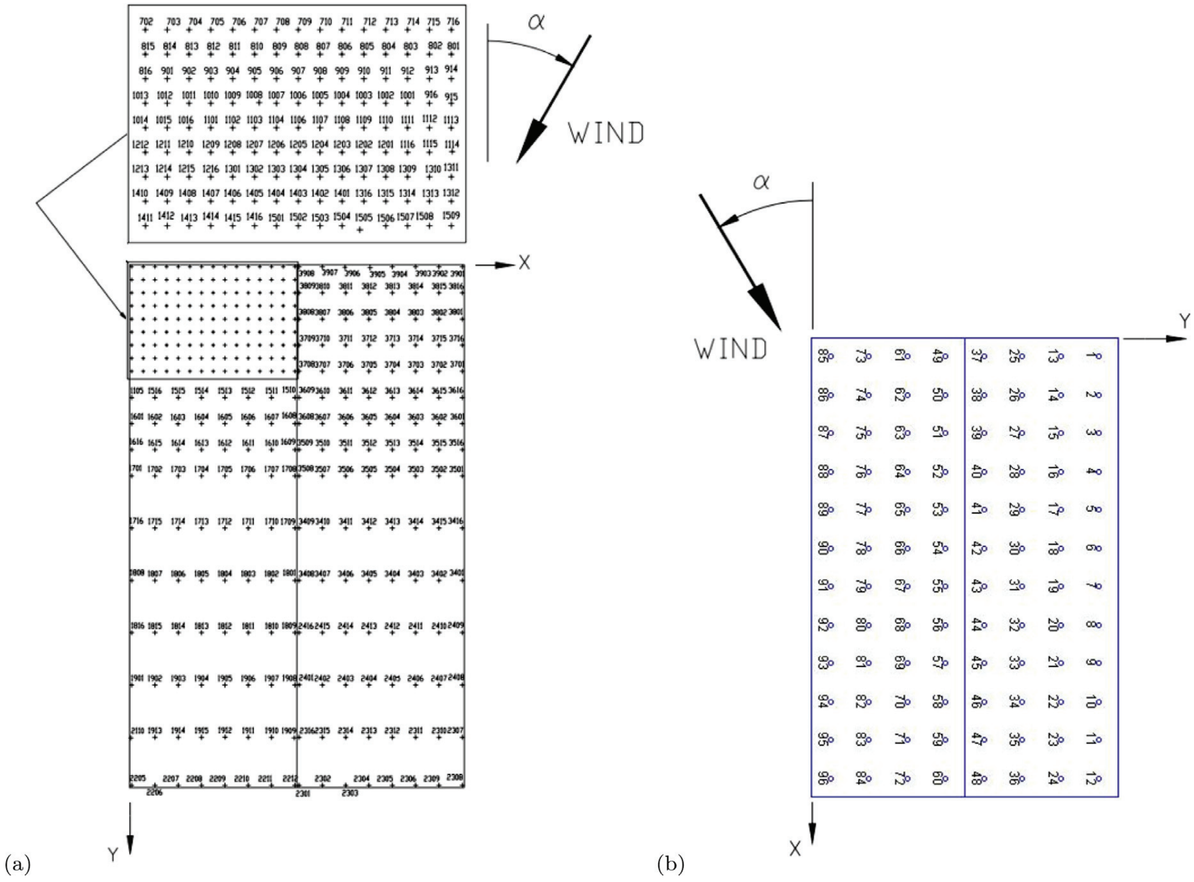

Fig. 1. Schematic diagram of pressure tap layout on the model building roof. (a) 335 pressure taps over the UWO building model with a dense patch of pressure taps installed at one corner; (b) 96 pressure taps uniformly distributed with a spacing of 20 mm over the TPU building model.

from each uncertainty source. This procedure is repeated through n iterations until the probability distribution of the outcomes is stable and well-defined. For example, for outcome distributions of a Gaussian nature, convergence criteria can be selected for the sample standard deviation u such that

$$\frac{|u_n - u_{n-1}|}{u_n} < 0.001 \tag{7}$$

A probabilistic interval can then be defined as the uncertainty in the result, typically a 95% level of coverage or 2σ. The process is depicted in Fig. 2. Using these results, the percent contribution of each identified elemental uncertainty to the overall measurement uncertainty of the quantity of interest can be evaluated. This study will estimate systematic measurement uncertainty of mean, standard deviation and peak pressure coefficients using instrument-level uncertainties of flow and pressure measurements.

Uncertainty quantification is performed for the UWO case only, because time series of point wind pressure in the TPU datasets were pre-treated with a moving average. The primary instruments used in the UWO wind-tunnel tests include a high-speed solid-state pressure scanning system for building surface pressure measurement, two HWAs and two pitot–static tubes for wind profiles (Ho et al., 2003, 2005). Introduced by such instruments to the UWO wind tunnel tests, four elemental uncertainty sources are identified: pressure tap U_p, pressure correlation among transducer channels $U_{p,corr}$, hot-wire accuracy $U_{V,acc}$ and hot-wire resolution $U_{V,res}$ in Table 2. For steady-state measurements, we commonly use equipment accuracy specification as the elemental source of uncertainty. Since no information is available about the pressure transducer model or the HWA, we have assumed that modern instruments' specifications are representative. The specifications of pressure scanner Scanivalve ZOC33 is used here: +/−10 inch H_2O pressure range (+/−52.023 psf), the accuracy specifications represent 2σ value and Gaussian distribution of errors (BIPM et al., 2008; Hubbard, 2019). The correlation error between pressure channels share the same calibration process and instrumentation, and therefore, share the systematic correlation uncertainty. A small level of correlation between pressure channels from pressure system calibration at 25% is used, typical of channel-to-channel calibration uncertainty ratios. For the HWA, the Kanomax Climomaster 6501 hot-wire velocity specifications are considered as representative and comparable to that used in the UWO tests. The four elemental uncertainties and assumed statistical distributions are summarized in Table 2.

Fig. 3 shows the flow charts of BL wind profile measurement uncertainties created by two hot-wires and two pitot tube measurements. The top of Fig. 3 represents the introduction of elemental uncertainties $U_{V,acc}$ and $U_{V,res}$ at different heights and their propagation with the hot-wire measurements. The bottom of Fig. 3 shows uncertainties of two pitot tube measurements as the parallel efforts. Both the total and static recordings of each pitot probe are needed to determine the dynamic pressures thus the velocity, so the elemental uncertainties of U_p and $U_{p,corr}$ are introduced and propagated through the data acquisition and reduction process.

Fig. 4 shows the elemental uncertainties U_p and $U_{p,corr}$ introduced by model pressure measurements (bottom chart), combined with uncertainties from the pitot tube measurements to obtain the re-referencing velocity ratios (top chart). The pitot tube measurements taken at the reference, intermediate and roof/eave heights contribute to the averaged V_H/V_{int} and V_{int}/V_{ref} (in Eqs. (3) and (4)). Two tests (one BL velocity profile and one model test) were performed and averaged to obtain V_{int}/V_H, and three test results (one BL velocity profile and

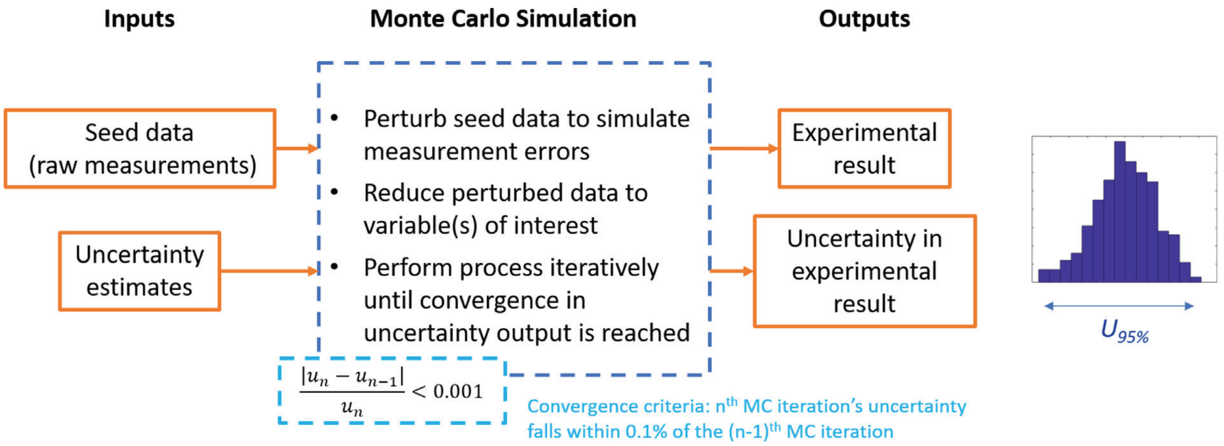

Fig. 2. Monte Carlo simulation of uncertainty propagation.

Table 2
Elemental uncertainty estimates and assumed statistical distributions.

Uncertainty quantity	Uncertainty source	Estimated uncertainty magnitude	Estimated uncertainty statistical distribution
U_p	Pressure scanner accuracy	±0.078 psf (±0.15%FS)	2σ, Gaussian distribution
$U_{p,corr}$	Pressure scanner calibration (channel to channel correlation)	±0.02 psf ($0.25U_P$)	2σ, Gaussian distribution
$U_{V,acc}$	Hot-wire accuracy	Greater of 2% of reading or 0.015 m/s	2σ, Gaussian distribution
$U_{V,res}$	Hot-wire resolution	±0.01 m/s	uniform distribution

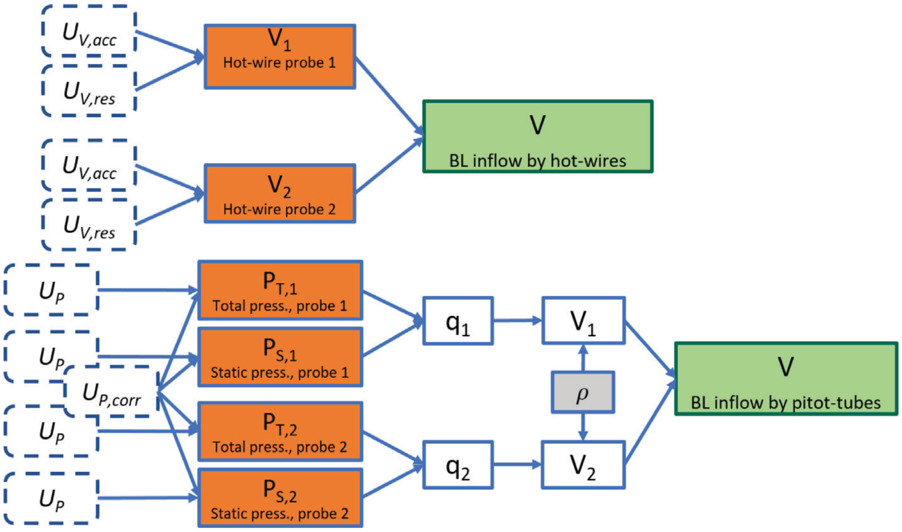

Fig. 3. Estimated uncertainties of measured parameters and the procedure to obtain BL inflow velocity profiles by parallel measurements with hot-wires and pitot tubes.

two model tests) were averaged to obtain V_{ref}/V_{int}. The velocity ratio measurements and averages from these tests are summarized in Table 3 of Ho et al. (2005). The velocity ratio uncertainties serve as the input to obtain U_{q_{ref}/q_H} in the bottom flow chart. All elemental uncertainties propagate from the point of measurement through the instruments, data acquisition and data reduction procedure to the primary variables of interest; $\overline{C_p}$, C'_p and $C_{p,peak}$.

3. Results and discussion

Incoming flow characteristics are crucial to examine the induced building wind load. We first compare the inflow characteristics of the UWO and TPU wind tunnels, the mean velocity profiles and turbulence intensities. Subsequently, we present the comparison of the pressure coefficients over the roof using the UWO and TPU wind-tunnel data in terms of mean and standard deviation, and expected peak pressure values at normal and cornering wind directions. For the UWO data, we included the measurement uncertainty quantification results for the roof and targeted locations.

3.1. Comparison of inflow characteristics

For wind-tunnel tests of low-rise building models, mostly wind properties in the atmospheric surface layer (or the lowest 10% of the ABL) are reproduced. The UWO full-scale reference wind speed is 13.7 m/s, with a 1:4 velocity ratio and wind-tunnel eave height velocity of 9.1 m/s. TPU full-scale reference wind speed is 22 m/s, with a 1:3 velocity ratio and wind-tunnel eave height velocity of 6.5 m/s. Inflow characteristics parameters were compared in lab-scale in Table 3. The

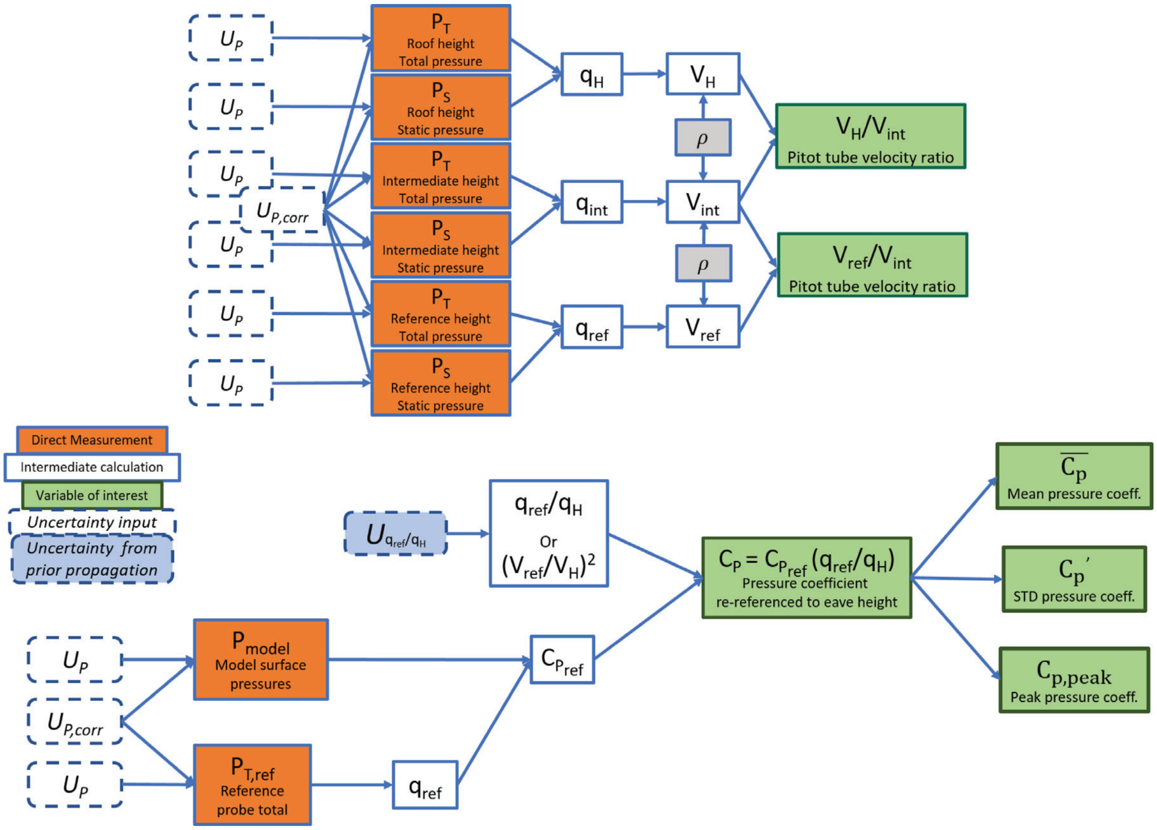

Fig. 4. Uncertainties of re-referencing velocity ratios (top chart) and building model surface pressure (bottom chart) to obtain the $\overline{C_p}$, C_p' and $C_{p,peak}$ in the UWO wind tunnel tests.

Table 3
Comparison of non-dimensional scaling parameters of the simulated surface-layer inflow of the UWO and TPU wind-tunnel tests.

Wind-tunnel Tests	Eave height velocity V_H (m/s)	Reynolds Number Re_H	Jensen number H/z_0
UWO	9.1	7.3×10^4	40.6
TPU	6.5	1.7×10^4	26.7 - 5.7

Reynolds number is defined as follows:

$$Re_H = \frac{V_H H}{\upsilon} \tag{8}$$

where H is the eave height, V_H is the eave height velocity and ν is the kinematic viscosity of air at the test pressure and temperature. Re_H are $7.3{\times}10^4$ and $1.7{\times}10^4$ for the UWO and TPU tests, respectively. For sharp-edged bluff bodies, such as low-rise buildings, a minimum Reynolds number of 10^4 is required to reduce the Reynolds number dependence (Cermak et al., 1999). Since the roughness height, z_o, associated with the simulated boundary-layer inflow in the TPU study was not specified, a range of 0.15 to 0.7 m based on the building codes is used to calculate the Jensen number (H/z_o) listed in Table 3 for a typical roughness height over the suburban terrain. A significant difference exists in the Jensen number of the UWO and TPU tests. The effects of Jensen Number on low-rise building pressure are discussed in Holmes and Carpenter (1990): fluctuating pressures decrease and mean suctions in separated flow regions increase with increasing Jensen number for the Jensen number between 120 and 480. While the Jensen numbers of the UWO/TPU tests are lower than the studied range of Jensen Numbers, the effects of variation of Jensen number on roof pressure statistics would be expected.

Fig. 5 shows the comparison of the mean inflow velocity ratio U/V_H and streamwise turbulent intensity T_u profiles between the UWO and TPU test cases. The power-law profile was used to fit a curve to the velocity ratio data, yielding power-law exponents of 0.23 for UWO and 0.21 for TPU and an R^2 value of 0.97. The UWO boundary-layer flow was described using the logarithmic law (Ho et al., 2003), thus no information of the power-law exponent was provided. The TPU boundary-layer flow is reported to have the exponent of 0.20 (Tamura, 2012), which closely matches the present estimate. Considerable differences in the velocity ratio and the streamwise turbulence intensity profiles are revealed in Fig. 5. The normalized velocity of the TPU tests is consistently less than that of the UWO tests above the eave height. This difference is almost negligible below the eave height. The streamwise turbulence intensities T_u show similar value of 0.25 below the roof height ($h/H = 1$). T_u is relatively constant below $h/H = 4$ for the TPU tests. In contrast, T_u decreases at a much higher rate with increasing the height h above the ground for the UWO test. At the eave height, $T_u = 0.22$ for UWO tests is lower than 0.25 of the TPU case. Turbulence intensity and turbulent scales of the incoming boundary-layer flows have significant impacts on spatial distribution and magnitude of the mean and fluctuating pressures (Morrison and Kopp, 2018; Fernández-Cabán and Masters, 2018). Differences in velocity profile, turbulence intensity level, Re_H along with the Jensen number need to be kept in mind when comparing pressure coefficients of the UWO and TPU cases in the following section.

3.2. Comparison of roof pressure statistics: $\overline{C_p}$, C_p' and $C_{p,peak}$ of the UWO and TPU cases

The overall distribution of roof pressure statistics of the low-rise building model for 90° and 45° wind directions are compared in Figs. 6 and 7. Fig. 6 displays contour plots of the mean $\overline{C_p}$, standard deviation C_p' and peak pressure coefficients $C_{p,peak}$ over the building roof subjected to the normal wind (90°) for the UWO and TPU tests.

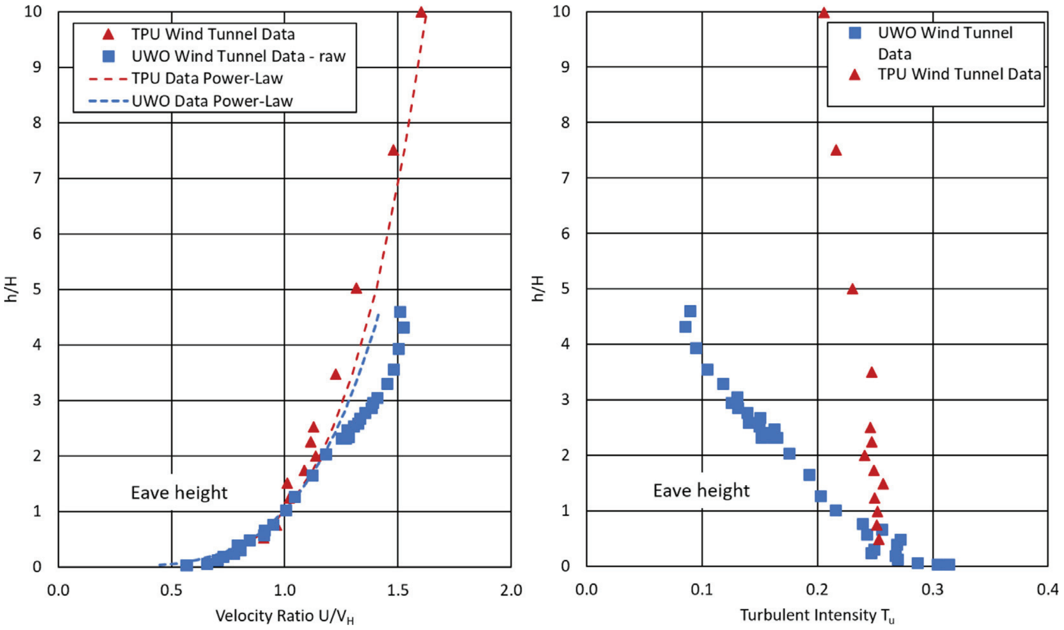

Fig. 5. Vertical profiles of mean wind profiles (left) and streamwise turbulence intensity (right) of the UWO and TPU wind-tunnel tests. Fitted power-law profiles are overlaid upon scattered raw data.

The lowest mean pressure coefficients $\overline{C_p}$ occur near the windward roof edge (Figs. 6(d) and 6(g)) where the approaching wind separates upon the sharp edge, then gradually increase as flow moves towards the roof trailing edge. Values of $\overline{C_p}$ over the entire roof surface are negative (Fig. 6(d) and 6(g)), yielding an uplift force collectively. The standard deviation of pressure coefficients C_p' (Figs. 6(e) and 6(h)) show higher values in the flow separation region and then reduced significantly. The peak pressure coefficients $C_{p,peak}$ (Figs. 6(f) and 6(i)) demonstrate the lowest values at the windward roof edge, and in particular the roof corner. Flow separation near the roof edge followed by the flow reattachment downstream is the dominant aerodynamic mechanism for the lowest mean pressure and the most severe peak suction for 90° wind (Akon and Kopp, 2016).

The spatial distribution of the mean, standard deviation and peak pressure coefficients ($\overline{C_p}$, C_p' and $C_{p,peak}$) of the UWO and TPU cases show a generally good agreement, but the magnitude should be studied in more details by comparing targeted locations (Figs. 8 and 9). The major difference is resulted from layout arrangement of pressure taps over the roof. The UWO building model is more densely populated with pressure taps compared to the TPU model, indicated by each marker in Fig. 1. Therefore, the pressure taps on the UWO model are able to capture the surface pressure with higher spatial resolution, including extreme values closer to the roof edge. Correspondingly, the pressure coefficient variation near the roof ridge ($x/H = 2$) become more distinct and visible in the UWO datasets.

The spatial distribution of roof pressure coefficients for a typical cornering wind of 45° is shown in Fig. 7. The overall pressure coefficient distribution for the UWO and TPU measurements agree well, demonstrating three distinct regions: the roof corner, along two windward roof edges and the pressure coefficient recovery region. Low $\overline{C_p}$ and $C_{p,peak}$ and high C_p' are at the roof corner. High values of C_p' and low $C_{p,peak}$ along the two edges reflect the distinct footprint of delta vortices. Due to coarsely spaced pressure taps (or lower spatial resolution) of the TPU data, the contour plots appear smoother than those of the UWO datasets. This also leads to that the regions of maximum and minimum values of pressure statistics are significantly reduced. In contrast, strong local non-discontinuity of pressure coefficient is evident near the roof ridge for the UWO measurements, which used two columns of pressure taps very close to the ridge (see markers on the UWO building model in Fig. 1).

To do a more detailed quantitative comparison, magnitudes of the $\overline{C_p}$, C_p' and $C_{p,peak}$ of the UWO and TPU data along the mid-span of the building for 90° wind are shown in Fig. 8. $\overline{C_p}$ of the TPU test case are consistently lower than that of UWO cases by 0.2 to 0.5. The difference in C_p' values across the mid-span of the models range between 0.03 and 0.1. The largest difference of 1 in $C_{p,peak}$ values is located around $x/H = 0.25$ and reduces as flow moves towards the trailing edge to around 0.1. The difference between the UWO and TPU test cases is more significant for $x/H < 1.5$, but becomes smaller for $x/H > 1.5$. The TPU measurements do not capture the peak suction near the leading edge due to a lower spatial resolution than that of UWO data. In the UWO data, one of the pressure coefficient data near the middle ridge does not follow the trend, most likely an outlier.

For 45° wind, the magnitudes of $\overline{C_p}$, C_p' and $C_{p,peak}$ measured by a series of pressure taps near the windward edge of the low building model is analyzed in Fig. 9. Though $\overline{C_p}$ show a similar trend between both cases, the TPU data is lower by 0.2 to 0.6 than those of UWO data. The lowest $\overline{C_p}$ of −1.25 in the UWO case was not captured in the TPU datasets. The C_p' values show a similar pattern, while the TPU data are consistently higher by 0.03 to 0.3. The $C_{p,peak}$ values of the TPU cases are consistently lower by 0.1 to 1.8 than that of the UWO results. Note that a slight difference of $x/H = 0.05$ exists between the locations of these taps of UWO and TPU models (Fig. 9), which might contribute to the pressure coefficient value difference.

The evident differences in the magnitude of $\overline{C_p}$, C_p' and $C_{p,peak}$ of the UWO and TPU cases (as seen in Figs. 8 and 9) are attributed to both the different inflow characteristics and the inherent measurement uncertainties of wind-tunnel model tests. Ideally, uncertainties of the UWO and TPU pressure coefficients are to be evaluated for a fair comparison. Because no raw pressure data are accessible from the TPU database, only the uncertainties of pressure coefficients for the UWO wind-tunnel tests are presented. The contours of the total measurement uncertainties for $\overline{C_p}$, C_p' and $C_{p,peak}$ are shown in the top row of Figs. 6 and 7. Note the total uncertainty refers to the sum of uncertainty values derived from the four identified uncertainty sources. The uncertainty levels are highest in the region where flow separates (for 90° wind) or delta vortices form (for 45° wind). It is not surprising that the lower peak pressure coefficients $C_{p,peak}$ are the greater of the uncertainties. Due to the heterogeneous distribution of roof pressure uncertainties,

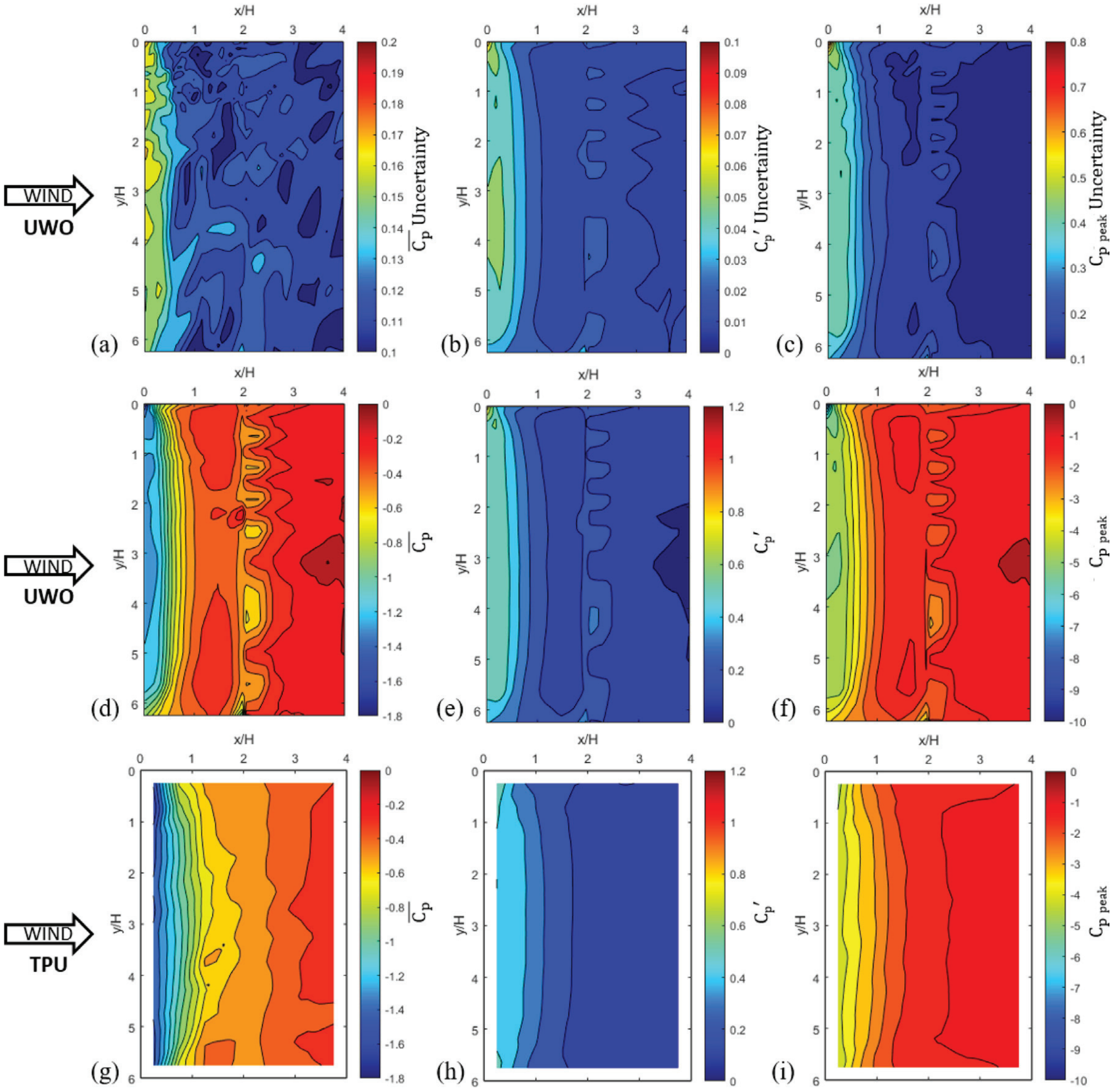

Fig. 6. Rooftop contour plots of $\overline{C_p}$ (left), C_p' (middle) and $C_{p,peak}$ (right) of the UWO (middle row) and TPU (bottom row) wind-tunnel tests at 90° wind direction. Measurement uncertainty contours of $\overline{C_p}$, C_p' and $C_{p,peak}$ of the UWO data are shown in the top row (a), (b) and (c).

the dominant uncertainty sources are expected to depend on the specific regions over a roof. Herein, driving measurement uncertainty sources are further assessed along the mid-span (Fig. 8) and the windward long-side edge (Fig. 9) for both the normal and cornering wind directions.

3.3. Driving measurement uncertainty sources

3.3.1. Roof mid-span at wind directions of 90° and 45°

Fig. 10 displays uncertainty percent contribution of each uncertainty source for $\overline{C_p}$, C_p', and $C_{p,peak}$ along the roof mid-span of the UWO model at 90° and 45° wind directions. The percent contributions herein are out of 100% of the total measurement uncertainty generated from the four elemental uncertainty sources. For the 90° case, the dynamic pressure ratio uncertainty U_{q_{ref}/q_H} and the building pressure tap uncertainty U_p are the two dominant uncertainty sources among four uncertainty sources for deriving the uncertainty of mean pressure coefficient $\overline{C_p}$ (Fig. 10(a) top row). The dynamic pressure ratio uncertainty U_{q_{ref}/q_H} shows the maximum (≈ 48%) at the roof leading edge as the leading uncertainty source and then reduces with increasing x/H. At $x/H = 2.5$, U_{q_{ref}/q_H} is negligible — about zero. In contrast, the second leading uncertainty source U_p, increases from about 40% to 90% (at $x/H = 2.5$), reaching a plateau beyond the location of $x/H = 2.5$. The reference probe dynamic pressure uncertainty $U_{q_{ref}}$ is about 5% and soon becomes negligible at $x/H = 0.75$. The correlation uncertainty $U_{p,corr}$ from the pressure transducer calibration holds a constant level of 5% at all tap locations. Uncertainties of $\overline{C_p}$ are more sensitive to U_{q_{ref}/q_H} at the leading edge where flow separates. Beyond this region, the overall $\overline{C_p}$ uncertainty is driven primarily by the building tap pressure measurement uncertainty U_p.

Uncertainty of standard deviation of pressure coefficient C_p' (Fig. 10(a) middle row) is dominated by the dynamic pressure ratio U_{q_{ref}/q_H} (90%) and $U_{q_{ref}}$ is about 10%, regardless of tap location. U_p and $U_{p,corr}$, the building and correlated pressure uncertainty contributions are negligible, since the only uncertainty propagated in this analysis applies as steady-state error, which drops out as part of the steady-state component of the C_p' calculation.

Similar to uncertainty of $\overline{C_p}$, $C_{p,peak}$ uncertainty (in Fig. 10(a) bottom row) is mostly from the dynamic pressure ratio uncertainty U_{q_{ref}/q_H} and the building pressure tap uncertainty U_p. U_{q_{ref}/q_H} decreases from about 80% at the leading edge to 15% to the trailing edge. The building pressure tap uncertainty U_p is insignificant at the leading edge, but

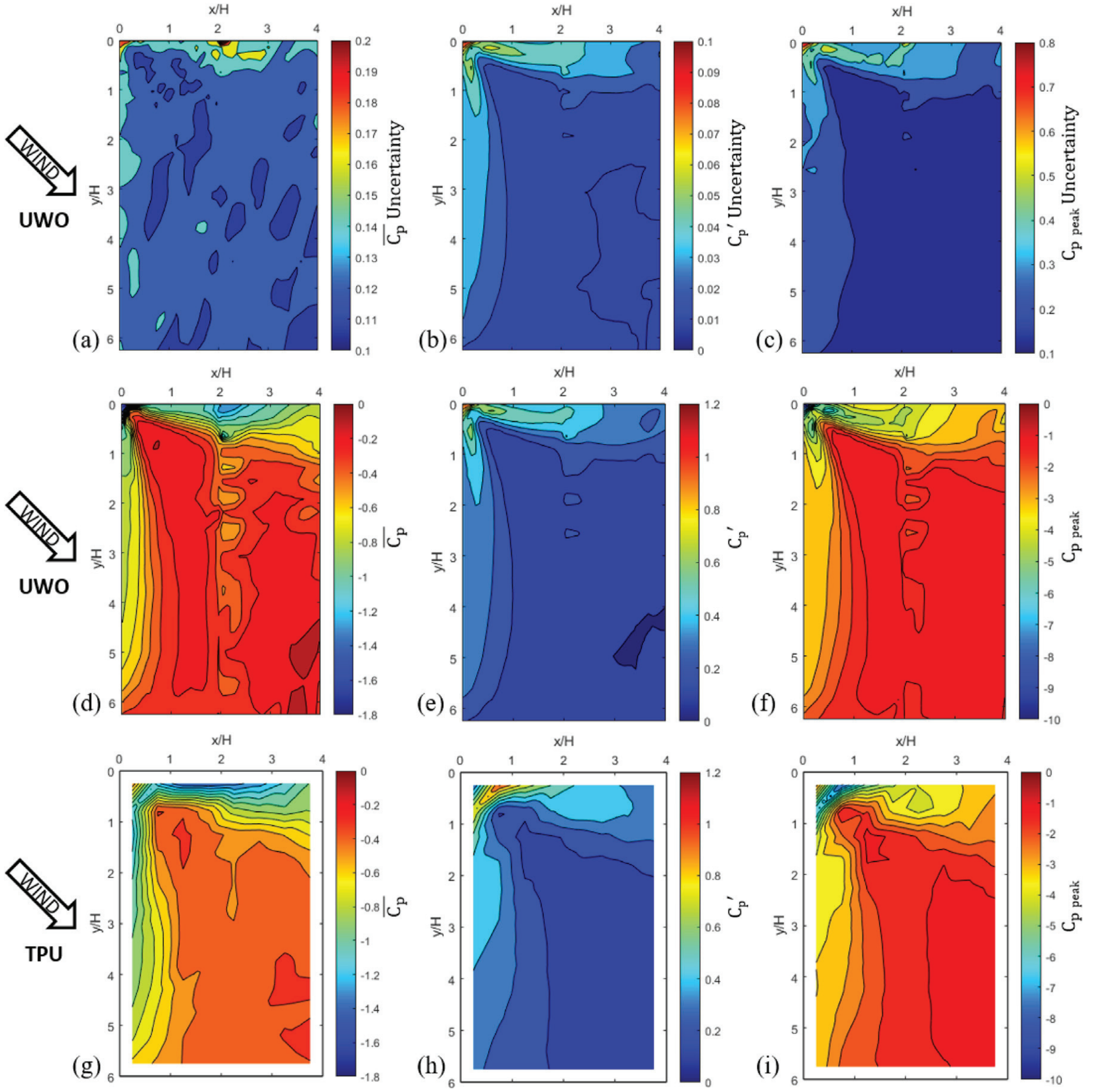

Fig. 7. Rooftop contour plots of $\overline{C_p}$ (left), C_p' (middle) and $C_{p,peak}$ (right) of the UWO (middle row) and TPU (bottom row) wind-tunnel tests at 45° wind direction. Measurement uncertainty contours of $\overline{C_p}$, C_p' and $C_{p,peak}$ of the UWO data are shown in the top row (a), (b) and (c).

gradually increases to be the dominant uncertainty (≈ 80%) at the trailing edge. The reference probe dynamic pressure uncertainty $U_{q_{ref}}$ is 15% at the leading edge and then declined to be about 10% beyond $x/H = 1.0$.

The most significant total uncertainty values lie with those of $C_{p,peak}$, with the maxim reaching up towards 0.80 at the roof corner for 45° wind direction (Fig. 7). Also, the maximum total uncertainty values for $\overline{C_p}$ are around 0.20 at the roof corner for 45° wind (top row of Fig. 7), indicating significance for consideration. As the foremost uncertainty source of uncertainties of $\overline{C_p}$, the building pressure tap uncertainty U_p is increased by around 26% at the leading edge at 45° wind compared to that of 90° wind. The dynamic pressure ratio uncertainty U_{q_{ref}/q_H} is reduced by about half at the leading edge compared to the 90° case, thus being the second driving uncertainty source. The reference probe dynamic pressure uncertainty $U_{q_{ref}}$ is decreased correspondingly. The uncertainties of C_p' and $C_{p,peak}$ remain relatively consistent for the two wind directions. The variations of uncertainty source contributions between 90° and 45° cases, are primarily due to the flow structure developed on the roof surface and captured by the pressure taps along the roof mid-span.

3.3.2. Wind-ward long-side roof edge at wind directions of 90° and 45°

Fig. 11 examines uncertainty percent contribution of each uncertainty source along the wind-ward long-side roof edge (marked in Fig. 9), because this location is strongly affected by the flow separation at the 90° wind, and by the delta-wing vortices for the 45° wind. Though two driving uncertainty sources are U_p and U_{q_{ref}/q_H} for the uncertainty of $\overline{C_p}$ (Fig. 11 top row), their percent contributions are noticeably different depending on the wind direction and the specific tap location. For the 45° case, the dominant source of the uncertainty of the $\overline{C_p}$ is building pressure tap uncertainty U_p. U_p starts at around 50% at the roof corner, jumping to about 90% at $y/H = 0.15$, then reducing to about 80% at $y/H = 1.2$ and downstream. The dynamic pressure ratio uncertainty U_{q_{ref}/q_H}, the second leading uncertainty source, exhibits a high level of around 37% at the roof upper-side edge attributed to delta vortices. U_{q_{ref}/q_H} drops to very low values (5%) at the following tap locations and then gradually increases to about 16% at $y/H = 1.2$. For the 90° wind direction, the primary uncertainty source for $\overline{C_p}$ uncertainty is the building pressure tap uncertainty U_p. U_p has a value of around 70% at the corner, then reduces to around 50% beyond $y/H = 0.35$. The secondary driver of $\overline{C_p}$ uncertainty is

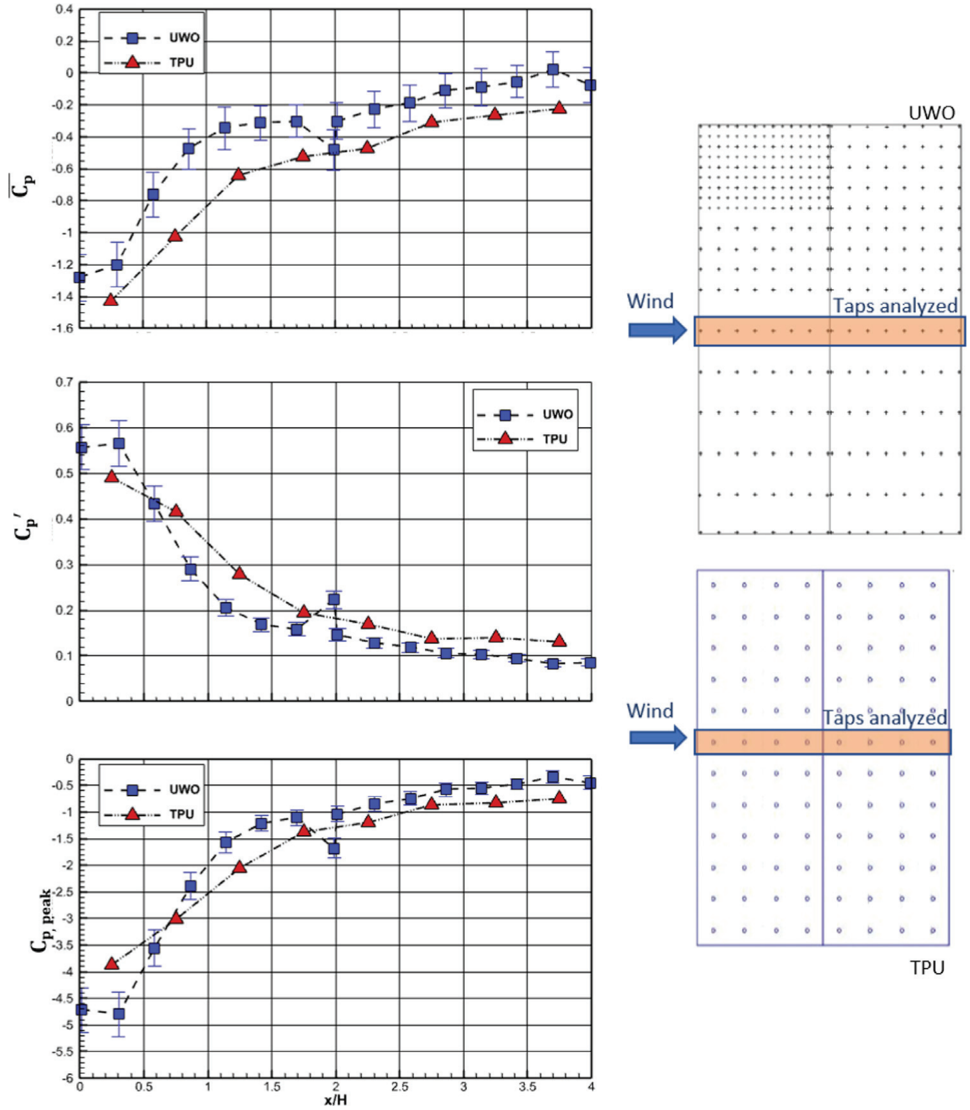

Fig. 8. Comparison of $\overline{C_p}$ (top), C_p' (middle) and $C_{p,peak}$ (bottom) along roof mid-span at 90° wind direction. Error bars indicate the measurement uncertainty levels of the UWO pressure coefficients.

the dynamic pressure ratio uncertainty U_{q_{ref}/q_H}, starting at around 23% then increasing to around 36% beyond $y/H = 0.35$.

Regardless of the wind direction, the correlated pressure uncertainty $U_{p,corr}$ and the reference probe dynamic pressure uncertainty $U_{q_{ref}}$ are minor uncertainty sources for the uncertainty of $\overline{C_p}$ (Fig. 11 top row). At 45° wind direction, $U_{p,corr}$ contributes at a relatively constant level of 10% in the column of the selected pressure tap array, and $U_{q_{ref}}$ contributes to around 6% in the corner, and reduces to less than 3% heading towards the trailing edge. At 90° wind direction, the correlation uncertainty $U_{p,corr}$ is slightly higher than the reference probe uncertainty (around 4%) at the corner, and remains relatively constant at around 6%.

The uncertainties of C_p' (Fig. 11 middle row) are impacted by only the dynamic pressure ratio uncertainty U_{q_{ref}/q_H} (≈ 83%) and the reference probe dynamic uncertainty $U_{q_{ref}}$ (≈ 16%) for the selected pressure taps. The two other uncertainty sources U_p and $U_{p,corr}$ mostly cancel out in the data reduction process. This remains unchanged for both wind directions.

For uncertainties of $C_{p,peak}$ at 45° wind direction (Fig. 11(b) bottom row), the dynamic pressure ratio uncertainty U_{q_{ref}/q_H} becomes the leading source, starting at around 80% at the corner, reducing to about 60% at $y/H = 0.35$, then increasing to about 73% beyond $y/H = 0.75$. The reference probe dynamic uncertainty $U_{q_{ref}}$ being the second leading source, is consistent at around 11%, followed by the building pressure tap uncertainty U_p around 6%. The correlation uncertainty $U_{p,corr}$ contributes at the lowest constant level, around 4%. At 90° wind direction, the $C_{p,peak}$ uncertainty follows the same driving uncertainty hierarchy as the 45° case, although with relatively constant levels of all uncertainty sources. The dynamic pressure ratio, reference probe dynamic pressure, building pressure tap and correlation uncertainties contribute to the $C_{p,peak}$ uncertainty around 80%, 13%, 5% and 2%, respectively.

3.4. Potential approaches to reduce measurement uncertainties

Once the driving uncertainty sources are determined, it is of great interest to think about how changes in data acquisition, instrumentation, and specific test procedure, might affect or reduce uncertainty. Since the driving uncertainty is the dynamic pressure ratio U_{q_{ref}/q_H} for the mean $\overline{C_p}$, standard deviation C_p', and peak pressure coefficients $C_{p,peak}$, improving the accuracy of turbulent velocities is essential to reduce the overall measurement uncertainties. Though pitot tubes have been standardized as a wind speed measurement probe, it is only reasonable to quantify the mean wind speed but hardly avoid

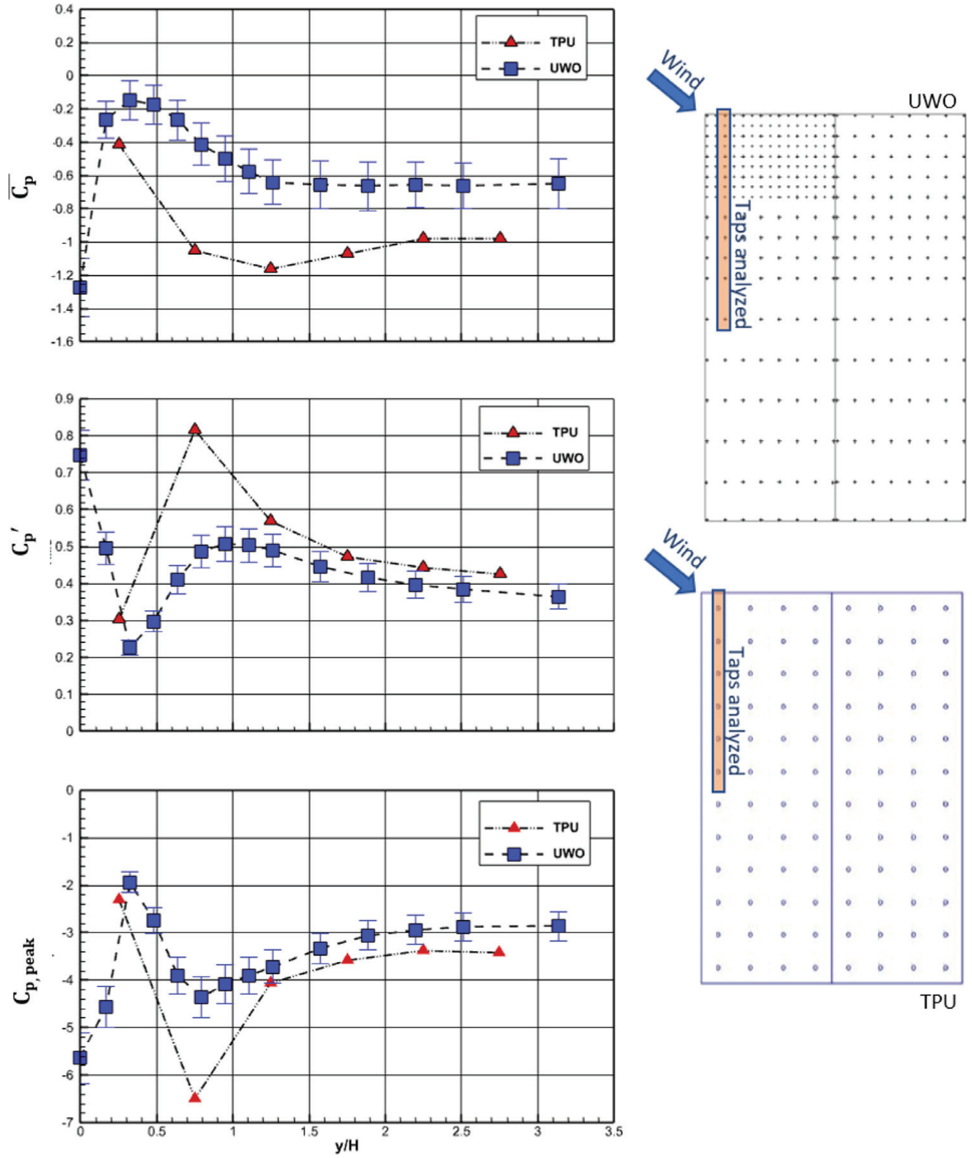

Fig. 9. Comparison of $\overline{C_p}$ (top), C_p' (middle) and $C_{p,peak}$ (bottom) near the windward roof edge at 45° wind direction. Error bars represent the measurement uncertainty levels of the UWO pressure coefficient.

disturbance of the sensitive flow near the roof edge. HWAs are appropriate to measure the turbulent velocities of inflows as documented in the UWO wind-tunnel tests but are tricky for the roof edge due to disturbance of the flow. The optics-based particle image velocimetry (PIV) has been an established technique to measure turbulent flow characteristics (Raffel et al., 2007). Indeed, in similar atmospheric BL wind tunnel experiments, PIV measurements have been used for wind turbine and wind farm wake aerodynamics research (Zhang et al., 2012, 2013; Markfort et al., 2018). PIV was also reported to examine the effects of turbulence on the mean roof pressure coefficients and reattachment lengths of separation bubbles for surface-mounted prisms in a BL wind tunnel (Akon and Kopp, 2016). The combination of PIV and HWAs for characterizing inflow velocity profile and quantify highly turbulent flows at the roof height while the model being present would reduce the measurement uncertainty of the pressure coefficient calculation compared to using pitot tubes. Moreover, in the UWO wind tunnel tests, pitot tube measurements at an intermediate level reference were used (Eq. (4)). The intermediate level measurement would introduce undesired uncertainties and thus should be avoided if possible.

Surface pressure tap uncertainty U_p is another dominant measurement uncertainty source of the mean $\overline{C_p}$ and peak pressure coefficients $C_{p,peak}$, though it does not impact uncertainties of C_p'. $U_{p,corr}$ is a secondary uncertainty source as long as pressure taps are used to measure the roof pressure. To explore alternatives, one possibility is to consider new surface pressure measurement techniques — for example a non-intrusive optics method pressure sensitive paint (PSP), which maps the surface pressure using images of paint response to pressure variation in the airflow. Various PSP methods, including the binary PSP and the fast-response PSP, have been extensively applied to aerospace or high-speed aerodynamics field (Liu and Sullivan, 2005; Crafton et al., 2013), but not to wind effects on model buildings yet. PSP allows the surface pressure to be measured with a very high spatial resolution corresponding to a single pixel of the scientific camera. However, the major challenge is the low signal-to-noise ratio for the airflow speed range that is of interest to the wind engineering community (Peng and Liu, 2020). Nevertheless, the PSP method is worthwhile to be further investigated for wind engineering applications. If this method is employed to replace most of the pressure taps, corresponding measurement uncertainties should be quantified.

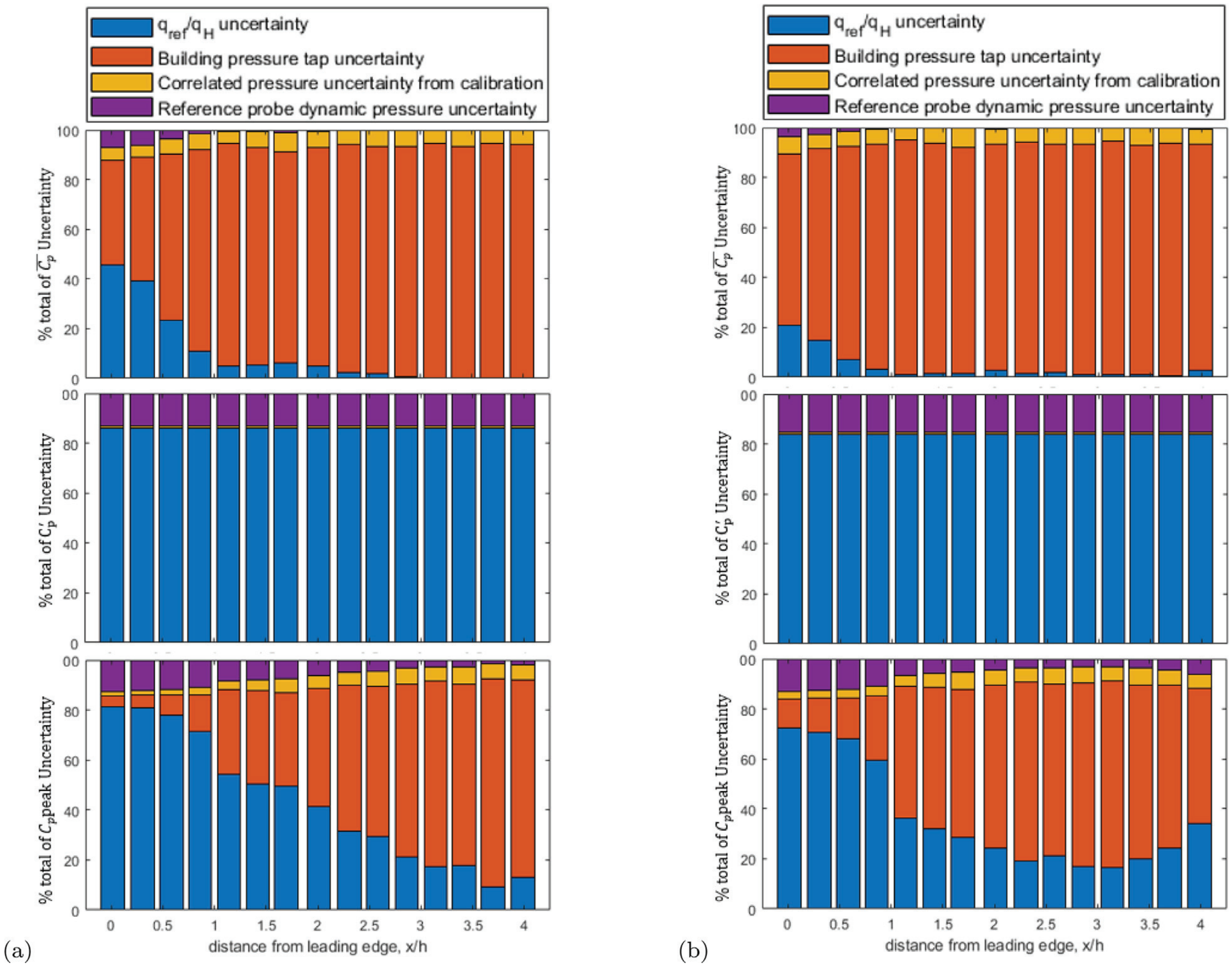

Fig. 10. Driving uncertainty sources of $\overline{C_p}$ (top), C_p' (middle), $C_{p,peak}$ (bottom) along roof mid-span of the UWO wind-tunnel tests at (a) 90° and (b) 45° wind directions.

4. Conclusions

The inconsistency of pressure coefficients reported from different BL wind tunnels has been acknowledged as a long-standing issue by the wind engineering community. It is important to understand what causes discrepancies of measured pressure coefficients from different wind tunnel tests since this is the primary means to determine pressure coefficients in the wind loading standards and codes. Uncertainty quantification of quantities of interest could shed light on the inconsistency issue and also allow for a meaningful comparison of results from different test facilities and with numerical model predictions. This work focuses on the measurement uncertainties by utilizing time series of roof pressure data for an isolated low-rise building model subjected to simulated BL inflows archived in the NIST and TPU aerodynamic databases. First, the mean, standard deviation and expected peak pressure coefficients were compared at the rooftop and targeted arrays of pressure taps for the normal and cornering wind directions. Second, a detailed uncertainty quantification analysis via the Monte Carlo simulation following the data acquisition and data reduction procedure was conducted for the UWO datasets. The roof pressure statistics from UWO/TPU wind tunnel tests show a consistent trend, however, the large differences in the roof pressure coefficient do not seem to be explained by the level of measurement uncertainties. The considerable differences of the inflow conditions, including the discrepancies in the velocity profile, turbulence intensity profile and the Jensen number, are expected to contribute to the pressure coefficient differences.

The level of measurement uncertainties is highly correlated with flow behavior over the roof surface. The highest uncertainties occur in the region of flow separation for the normal wind and delta vortices for the cornering wind. Among the four identified measurement uncertainty sources used for the bias uncertainty quantification, two major uncertainty sources – the dynamic pressure ratio U_{q_{ref}/q_H} and the building surface pressure uncertainties U_p – contribute most to the $\overline{C_p}$ and $C_{p,peak}$. The weight of the two leading uncertainty sources depends on the wind direction and the specific location of a pressure tap. For the uncertainties of standard deviation pressure coefficient C_p', the dynamic pressure ratio uncertainty U_{q_{ref}/q_H} remain to be the dominant uncertainty source with the reference probe dynamic pressure uncertainty $U_{q_{ref}}$ as the second. Alternative measurement methods such as PIV and PSP, can be considered to potentially reduce the dynamic pressure ratio U_{q_{ref}/q_H} and the building surface pressure uncertainties U_p, respectively.

The present uncertainty quantification focuses on the systematic errors, specifically the measurement and data reduction uncertainties, which are important when comparing different wind tunnel tests and as a reference for CFD validation. Ideally, random errors should also be evaluated if details of the flow facility, environmental factors are available. Once the driving uncertainty sources are correctly identified, a new set of experiments can be conducted to compensate for these aspects. The current uncertainty analysis does not account for interaction between different uncertainties, which is the limitation of this approach (Stephens et al., 2016). It should also be noted, uncertainty results are only as good as the elemental uncertainty estimates that are propagated through the specific data acquisition and data reduction procedure. The more pertinent data are for the random, systematic, and spatial

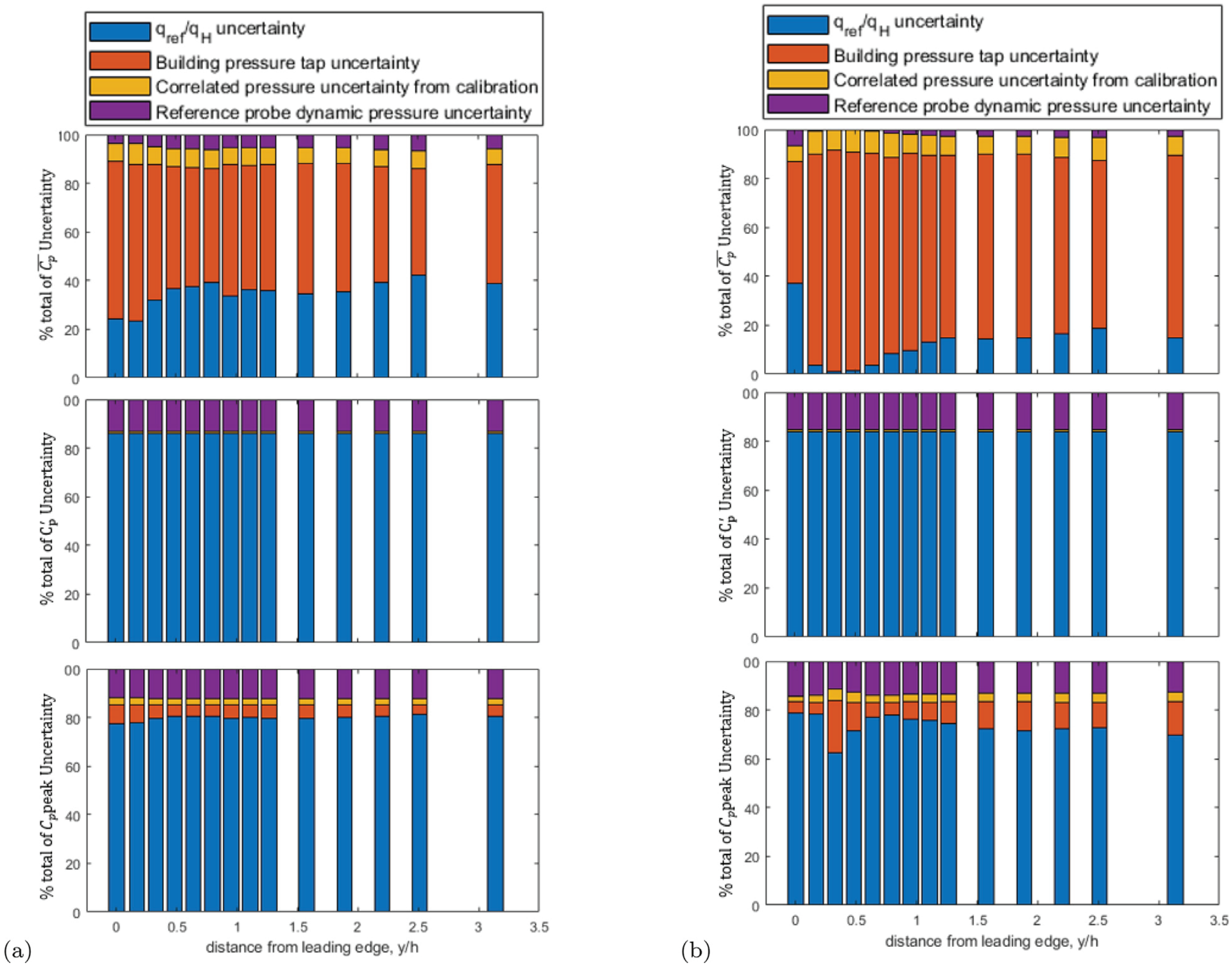

(a) (b)

Fig. 11. Driving uncertainty sources of $\overline{C_p}$ (top), C_p' (middle), $C_{p,peak}$ (bottom) near the windward roof edge of the UWO wind-tunnel tests at (a) 90° and (b) 45° wind directions.

distribution of uncertainty estimates, the more reliable the uncertainty analysis is. This work only accounts for measurement uncertainties of UWO results by propagating measurement device uncertainties. Other uncertainty sources, including model surface effects, tap-to-tap effects and static tap finish condition (dimension, edge characteristics like chamfers, blemishes, etc.) are difficult to quantify and not taken into account. If these uncertainty contributors could be estimated, the uncertainty bounds of the UWO datasets are expected to expand. This work intends to improve understanding of critical uncertainty sources of the pressure measurements in the BL wind tunnel of the UWO aerodynamics datasets, shedding light on why the significant discrepancy exists between pressure statistics results from different facilities.

CRediT authorship contribution statement

Erick Shelley: Data analysis, Writing – original draft, Writing – review & editing. **Erin Hubbard:** Data analysis, Methodology, Data visualization, Investigation. **Wei Zhang:** Conceptualization, Funding acquisition, Investigation, Validation, Writing – review & editing.

Declaration of competing interest

The authors declare that they have no known competing financial interests or personal relationships that could have appeared to influence the work reported in this paper.

Data availability

Data will be made available on request.

Acknowledgments

E. Shelley and E. Hubbard acknowledge the generous support of Ohio Space Grant Consortium (OSGC), United States of America Internship program and the Master's OSGC Fellowship, United States of America. W. Zhang acknowledges the support of the National Science Foundation (NSF), United States of America CAREER grant (Award# 1944776) and the CSU Faculty Research Development Funds, United States of America.

References

Akon, A.F., Kopp, G.A., 2016. Mean pressure distributions and reattachment lengths for roof-separation bubbles on low-rise buildings. J. Wind Eng. Ind. Aerodyn. 155, 115–125.

BIPM, I., IFCC, I., Iupac, I., 2008. Evaluation of measurement data-supplement 1 to the'guide to the expression of uncertainty in measurement. In: Propagation of Distributions using A Monte Carlo Method.

Cermak, J.E., 2003. Wind-tunnel development and trends in applications to civil engineering. J. Wind Eng. Ind. Aerodyn. 91 (3), 355–370.

Cermak, J.E., et al., 1999. Wind Tunnel Studies of Buildings and Structures. American Society of Civil Engineers (ASCE).

Cochran, L., 2006. State of the art review of wind tunnels and physical modelling to obtain structural loads and cladding pressures. Archit. Sci. Rev. 49 (1), 7–16.

Coleman, H.W., Steele, W.G., 2018. Experimentation, Validation, and Uncertainty Analysis for Engineers. John Wiley & Sons.

Crafton, J., Fonov, S., Forlines, R., Palluconi, S., 2013. Development of pressure-sensitive paint systems for low speed flows and large wind tunnels. In: 51st AIAA Aerospace Sciences Meeting Including the New Horizons Forum and Aerospace Exposition 2013. http://dx.doi.org/10.2514/6.2013-482.

Endo, M., Bienkiewicz, B., Ham, H., 2006. Wind-tunnel investigation of point pressure on TTU test building. J. Wind Eng. Ind. Aerodyn. 94 (7), 553–578.

Fernández-Cabán, P.L., Masters, F.J., 2018. Effects of freestream turbulence on the pressure acting on a low-rise building roof in the separated flow region. Front. Built Environ. 4, 17.

Fritz, W.P., Bienkiewicz, B., Cui, B., Flamand, O., Ho, T.C., Kikitsu, H., Letchford, C.W., Simiu, E., 2008. International comparison of wind tunnel estimates of wind effects on low-rise buildings: Test-related uncertainties. J. Struct. Eng. 134 (12), 1887–1890. http://dx.doi.org/10.1061/(ASCE)0733-9445(2008)134:12(1887).

Gavanski, E., Gurley, K.R., Kopp, G.A., 2016. Uncertainties in the estimation of local peak pressures on low-rise buildings by using the Gumbel distribution fitting approach. J. Struct. Eng 142 (11), 04016106.

Gierson, M., Phillips, B., Duthinh, D., 2015. Evaluation of ASCE 7-10 wind velocity pressure coefficients on the components and cladding of low-rise buildings using recent wind tunnel testing data. In: 6th Int. Conf. on Advances in Experimental Structural Engineering, and 11th Int. Workshop on Advanced Smart Materials and Smart Structural Technology, Univ. of Illinois, Urbana, IL.

Hagos, A., Habte, F., Chowdhury, A.G., Yeo, D., 2014. Comparisons of two wind tunnel pressure databases and partial validation against full-scale measurements. J. Struct. Eng. 140 (10), 04014065. http://dx.doi.org/10.1061/(asce)st.1943-541x.0001001.

Ho, T.C.E., Surry, D., Morrish, D., 2003. NIST/TTU Cooperative Agreement–Windstorm Mitigation Initiative: Wind Tunnel Experiments on Generic Low Buildings. Univ. of Western Ontario, London, on, Canada.

Ho, T.C.E., Surry, D., Morrish, D., Kopp, G.A., 2005. The UWO contribution to the NIST aerodynamic database for wind loads on low buildings: Part 1. Archiving format and basic aerodynamic data. J. Wind Eng. Ind. Aerodyn. 93 (1), 1–30. http://dx.doi.org/10.1016/j.jweia.2004.07.006.

Holmes, J., 1988. Distribution of peak wind loads on a low-rise building. J. Wind Eng. Ind. Aerodyn. 29 (1–3), 59–67.

Holmes, J.D., Carpenter, P., 1990. The effect of jensen number variations on the wind loads on a low-rise building. J. Wind Eng. Ind. Aerodyn. 36, 1279–1288.

Hubbard, E.P., 2019. Uncertainty analysis of the CE-22 advanced nozzle test facility. Tech. rep..

Kareem, A., Tamura, Y., 2013. Advanced Structural Wind Engineering. Vol. 482, Springer.

Kopp, G.A., Morrison, M.J., 2018. Component and cladding wind loads for low-slope roofs on low-rise buildings. J. Struct. Eng. 144 (4), 04018019.

Lamberti, G., Gorlé, C., 2018. Uncertainty quantification for RANS predictions of wind loads on buildings. In: Conference of the Italian Association for Wind Engineering. Springer, pp. 402–412.

Letchford, C., 2001. Wind loads on rectangular signboards and hoardings. J. Wind Eng. Ind. Aerodyn. 89 (2), 135–151.

Liu, T.T., Sullivan, J.P., 2005. Pressure and Temperature Sensitive Paints. Springer, p. 328.

Markfort, C.D., Zhang, W., Porté-Agel, F., 2018. Analytical model for mean flow and fluxes of momentum and energy in very large wind farms. Bound.-Lay. Meteorol. 166 (1), 31–49.

Morrison, M.J., Kopp, G.A., 2018. Effects of turbulence intensity and scale on surface pressure fluctuations on the roof of a low-rise building in the atmospheric boundary layer. J. Wind Eng. Ind. Aerodyn. 183, 140–151.

Nandi, T.N., Pintar, A.L., Simiu, E., 2022. Influence of surface roughness uncertainties on design of structures with open and suburban exposures. ASCE-ASME J. Risk Uncertain. Eng. Syst. A 8 (1), 04021068.

NIST, 2017. NIST aerodynamic database. https://www.nist.gov/el/materials-and-structural-systems-division-73100/nist-aerodynamic-database.

Oh, J.H., Kopp, G.A., Inculet, D.R., 2007. The UWO contribution to the NIST aerodynamic database for wind loads on low buildings: Part 3. Internal pressures. J. Wind Eng. Ind. Aerodyn. 95 (8), 755–779.

Peng, D., Liu, Y., 2020. Fast pressure-sensitive paint for understanding complex flows: from regular to harsh environments. Exp. Fluids 61 (1), 1–22.

Raffel, M., Willert, C.E., Kompenhans, J., et al., 2007. Particle Image Velocimetry: a Practical Guide. Vol. 2.

Sadek, F., Simiu, E., 2002. Peak non-Gaussian wind effects for database-assisted low-rise building design. J. Eng. Mech. 128 (5), 530–539. http://dx.doi.org/10.1061/(asce)0733-9399(2002)128:5(530).

Scharnowski, S., Kähler, C.J., 2020. Particle image velocimetry-classical operating rules from today's perspective. Opt. Lasers Eng. 135, 106185.

Simiu, E., Yeo, D., 2019. Wind Effects on Structures: Modern Structural Design for Wind. John Wiley & Sons.

Simiu, E., et al., 2009. Toward a standard on the wind tunnel method. NIST report.

St. Pierre, L., Kopp, G., Surry, D., Ho, T., 2005. The UWO contribution to the NIST aerodynamic database for wind loads on low buildings: Part 2. Comparison of data with wind load provisions. J. Wind Eng. Ind. Aerodyn. 93 (1), 31–59.

Stephens, J., Hubbard, E., Walter, J., McElroy, T., 2016. Uncertainty analysis of NASA glenn's 8-by 6-foot superonic wind tunnel. In: 54th AIAA Aerospace Sciences Meeting. p. 1148.

Surry, D., 1991. Pressure measurements on the texas tech building: wind tunnel measurements and comparisons with full scale. J. Wind Eng. Ind. Aerodyn. 38 (2–3), 235–247.

Tamura, Y., 2012. Aerodynamic Database for Low-Rise Buildings. Global Center of Excellence Program, Tokyo Polytechnic Univ., Tokyo, Japan.

Tieleman, H.W., 2003. Wind tunnel simulation of wind loading on low-rise structures: a review. J. Wind Eng. Ind. Aerodyn. 91 (12–15), 1627–1649.

TPU, 2012. TPU aerodynamic database. http://wind.arch.t-kougei.ac.jp/system/eng/contents/code/tpu.

Zhang, W., Markfort, C.D., Porté-Agel, F., 2012. Near-wake flow structure downwind of a wind turbine in a turbulent boundary layer. Exp. Fluids 52 (5), 1219–1235.

Zhang, W., Markfort, C., Porté-Agel, F., 2013. Wind-turbine wakes in a convective boundary layer: a wind-tunnel study. Bound.-Lay. Meteorol. 146 (2), 161–179. http://dx.doi.org/10.1007/s10546-012-9751-4.